Received: 8 March 2021 | Revised: 23 July 2021 | Accepted: 23 July 2021

DOI: 10.1096/fj.202100323RR

THE FASEB JOURNAL

RESEARCH ARTICLE

X-ray microtomography reveals a lattice-like network within aortic elastic lamellae

Aïcha Ben Zemzem[1] | **Aline Genevaux**[1] | **Amandine Wahart**[1] | **Andrew J. Bodey**[2] | **Sébastien Blaise**[1] | **Béatrice Romier-Crouzet**[1] | **Jessica Jonquet**[1] | **Camille Bour**[1] | **Rémi Cogranne**[3] | **Pierre Beauseroy**[3] | **Manuel Dauchez**[1] | **Michael J. Sherratt**[4] | **Laurent Debelle**[1,4] | **Sébastien Almagro**[1]

[1]CNRS UMR7369 MEDyC, University of Reims Champagne-Ardenne, Reims, France

[2]Diamond Light Source, Oxfordshire, UK

[3]Troyes University of Technology, UMR CNRS 6281 ICD/ROSAS/LM2S, Troyes, France

[4]Division of Cell Matrix Biology and Regenerative Medicine, School of Biological Sciences, Faculty of Biology Medicine and Health, The University of Manchester, Manchester, UK

Correspondence
Sébastien Almagro, CNRS UMR7369 MEDyC, University of Reims Champagne-Ardenne, 51100 Reims, France.
Email: sebastien.almagro@univ-reims.fr

Funding information
DLS, Grant/Award Number: MT12776; University of Reims Champagne-Ardenne; DRRT of Champagne-Ardenne; Centre National de la Recherche Scientifique (CNRS)

Abstract

The arterial wall consists of three concentric layers: intima, media, and adventitia. Beyond their resident cells, these layers are characterized by an extracellular matrix (ECM), which provides both biochemical and mechanical support. Elastin, the major component of arterial ECM, is present in the medial layer and organized in concentric elastic lamellae that confer resilience to the wall. We explored the arterial wall structures from C57Bl6 (control), *db*/*db* (diabetic), and $ApoE^{-/-}$ (atherogenic) mice aged 3 months using synchrotron X-ray computed microtomography on fixed and unstained tissues with a large image field (8 mm^3). This approach combined a good resolution (0.83 μm/voxel), large 3D imaging field. and an excellent signal to noise ratio conferred by phase-contrast imaging. We determined from 2D virtual slices that the thickness of intramural ECM structures was comparable between strains but automated image analysis of the 3D arterial volumes revealed a lattice-like network within concentric elastic lamellae. We hypothesize that this network could play a role in arterial mechanics. This work demonstrates that phase-contrast synchrotron X-ray computed microtomography is a powerful technique which to characterize unstained soft tissues.

KEYWORDS

aorta, elastic lamellae, elastin, synchrotron X-ray micro-computed tomography

1 | INTRODUCTION

In the vascular system of mammals, elastic arteries play a key physiological role. They distribute blood to the entire body following cardiac ejection and soften the initial pressure surge by inflating and recoiling to help maintain a constant pressure.[1] This elastic behavior, which is critical for proper vascular function, is due to the presence

Abbreviations: ECM, extracellular matrix; EEL, external elastic lamella.; EL, elastic lamellae.; IEL, internal elastic lamella.; MicroCT, micro computed tomography.

Aïcha Ben Zemzem and Aline Genevaux are contributed equally to this work.

This is an open access article under the terms of the Creative Commons Attribution-NonCommercial-NoDerivs License, which permits use and distribution in any medium, provided the original work is properly cited, the use is non-commercial and no modifications or adaptations are made.
© 2021 The Authors. *The FASEB Journal* published by Wiley Periodicals LLC on behalf of Federation of American Societies for Experimental Biology

of concentric elastic lamellae (EL) within the vessel wall which bestow resilience and compliance to the tissue.

In the arterial wall, elastic lamellae are found in the *tunica media* layer. They are made of an elastic macropolymer, named elastin, characterized by its extreme stability and hydrophobicity. Elastin chains are extensively cross-linked and present a high conformational entropy, which is thought to be important in mediating elastic recoil.[2] At the transmission electron microscopy level, cross-linked elastin in fibers and lamellae is described as an amorphous polymer devoid of any internal structure.[2]

The half-life of elastin is estimated to be 70 years in humans[3] but despite this exceptional persistence, the elastin network is subject to age-related fragmentation in diseases (atherosclerosis, diabetes) and genetic disorders (Marfan and Williams-Beuren syndrome). Typically, in such cases, EL appear fragmented and locally thickened or thinned. Such aberrant remodeling of medial EL is associated with hypertension, heart failure, stroke, renal failure, or aneurysm formation.[4] The occurrence of these pathologies increases morbidity and reduces life expectancy. However, the complexity of arterial wall remodeling in both aging and vascular disease has, so far, ensured that the causative mechanisms and molecular consequences remain poorly defined.

Commonly, characterization of arterial wall remodeling relies primarily on the assessment of 2D tissue sections used to reconstruct the 3D micro-morphology. However, optical and transmission electron microscopy techniques are inherently prone to loss of data because sections are fragile.[5] Additionally, common 3D imaging techniques such as confocal and two-photon microscopy are limited to thin sections leading to restricted image volume and contrast. Therefore, our understanding of the 3D structure, and hence, the mechanical function of healthy elastic arteries is crucially dependent on the chosen imaging techniques. Since the elastic properties of arteries are conferred by the whole arterial wall, a more complete understanding of vascular wall architecture and its evolution during aging requires methods allowing 3D imaging of large vessel samples without sectioning.

In 2015, we demonstrated[6] that it is possible to resolve arterial microstructure using "laboratory" (microfocus tube) phase contrast microCT imaging in unpressurized and pressurized carotid arteries (from young, healthy rats) with an effective voxel size of 0.75 μm. Recently, we have shown that synchrotron-based phase contrast microCT can facilitate the measurement of statistically-significant differences in the wall structure of aorta from aged, healthy, and Marfan syndrome model mice.[7]

In this work, we performed synchrotron-based phase contrast microCT imaging of aorta in order to produce a detailed description of arterial features (high resolution) before the onset of vascular remodeling in 3 mice models (normal, diabetic, and atherogenic-prone). The high flux and coherence of the I13-2 beamline at the Diamond Light Source synchrotron enabled enhanced throughput, good signal/noise imaging with inline phase contrast. In order to avoid any imaging bias in favor of specific components due to differential staining, these samples were imaged in the absence of contrasting agents. Here, we present 3D reconstructions of large aortic segments and discuss the structures visualized by phase contract microCT with reference to current understanding of vascular structures and function.

2 | MATERIAL AND METHODS

2.1 | Animals

Mice from three strains sharing the same genetic background were used: C57Bl6J (normal), *db/db* (diabetic), and $ApoE^{-/-}$ (atherogenic-prone). Animal procedures were performed in accordance with the Guide for the Care and Use of Laboratory Animals of the US National Institutes of Health and were approved by the Animal Subjects Committee of Champagne Ardenne. 12-week-old C57BL6J, *db/db,* and $ApoE^{-/-}$ mice (n = 5/group) were purchased from Charles River (Ecully, France) and caged in a 12:12 hour light/dark cycle in a temperature- and humidity-controlled environment. All mice were allowed ad libitum access to diet and water during the experimental period. Mice were fed with a normal diet (ND, AIN-93M rodent diet, Special Diet Service, UK).

2.2 | Mouse aorta sample preparation

After sacrifice, around 2 cm of their aortic segment (upper part near arch, descending thoracic aorta, and abdominal aorta) were dissected. The surrounding tissue of the aorta was kept. Samples were further chemically fixed in 4% formaldehyde, dehydrated, and embedded in paraffin.

2.3 | Synchrotron X-ray tomography

Tomography was performed at the Diamond-Manchester Imaging Branchline I13-2[8,9] of the Diamond Light Source (DLS) synchrotron (Oxfordshire, United Kingdom). A partially-coherent, near-parallel, polychromatic "pink" beam (circa 8-30 keV) was generated by an undulator in an electron storage ring of 3.0 GeV voltage and 300 mA current. For data collection, the undulator gap was set to 5.0 mm. The beam was reflected from the platinum stripe of a grazing-incidence focusing mirror and high-pass filtered with 1.3 mm pyrolytic graphite, 3.2 mm aluminum, and

70 μm steel, resulting in a beam of weighted-mean photon energy of ~29 keV. Slits were used to restrict the beam just outside the field of view; this limited both sample exposure and the intensity of noise arising from scintillator defects. Samples were placed on a HUBER 1002 manual goniometer (HUBER Diffraktionstechnik GmbH & Co., Germany), mounted on perpendicular Newport MFA-PPD (Newport Corp., USA) linear stages, atop an Aerotech ABRT-260 (Aerotech Inc, USA) rotation stage. Various propagation distances were trialed, and ~100 mm was chosen to give a sufficient level or phase contrast. 8,001 projections were acquired at equally spaced angles over 180° of continuous rotation ("fly scan"), with an extra projection (not used for reconstructions) collected at 180° to check for possible sample deformation, bulk movements, and beam damage relative to the first (0°) projection. Projections were collected by a pco.edge 5.5 (PCO AG, Germany) detector (sCMOS sensor of 2560 × 2160 pixels) mounted on a visual light microscope of variable magnification. Magnification was controlled via rotation of a turret incorporating various scintillator-coupled objective lenses. A 4× objective, coupled to a 500 μm $CdWO_4$ scintillator, mounted ahead of a 2× lens provided 8× total magnification, a field of view of 2.1 × 1.8 mm, and an effective pixel size of 0.8125 μm. Prior to reconstruction via filtered back projection, projection images were flat- and dark-field corrected, and ring artifact suppression was performed.[10]

2.4 | Software and visualization

Basic image and video manipulation were performed with ImageJ[11] as well as 3D volumetric visualization figures and videos using the ImageJ 3D Viewer plugin. Our image analysis software was scripted with *Matlab* (MathWorks, Natick, MA, USA) including VP/CF/IP/DM/SG/ST toolboxes. Some video sequences were realized with *Amira for Life & Biomedical Sciences* (Thermo Fisher Scientific, Waltham, MA, USA). Videos were encoded in MP4 with the open-source video transcoder *HandBreak* (https://handbrake.fr/).

Before entering the image analysis pipeline, the 3D reconstructions realized from the recorded scans were checked for preparation artefacts such as bubbles in the lumen or huge blood clots. Scans exhibiting such features were discarded. In addition, we did not consider stacks where the signal/noise ratio was poor, making reliable automated image processing impossible.

2.5 | Image analysis

The computer used for this work was a dual processor Intel Xeon E5 2680 V2 (2 × 10 cores) with 128 GB RAM, high speed SSD disks, and a NVIDIA GeForce 2080Ti with 11Gb of RAM. Whenever possible, Matlab computing was parallelized with the dedicated toolbox on 20 cores. Three hours were necessary to compute the segmentation of 1500 × 1500 × 2500 stacks. Measurements of elastic structures took about 3 hours for 200 images. Briefly, 16 bit-depth TIFF stacks were first reduced to 8-bit manually using ImageJ by selecting a subset of the dynamic range that provides the best contrast for elastic structures. In rare cases, if extra-bright artefacts considerably reduced the 16-bit image dynamic, we created a Matlab script that identified the well exposed images, extracted their 16-bit histograms, and created a reference average histogram from all of them. The badly exposed images were also spotted, very bright artefacts were localized, and removed, thus their new histograms were computed again and transformed to fit the reference.

Segmentation of images was realized in several steps. First, for each image, an iterative process found the best threshold value to obtain a closed nearly circular structure of a sufficient surface that corresponded to an approximation of the aorta. Once found, the lumen was then easily segmented and the aortic wall mask was deduced. If not found, the image was labeled "empty." The presence of blood clot inside the lumen could produce this kind of "empty" result. Dimensions of all masks were then analyzed statistically to eliminate extremely small or huge ones, which were labeled "empty." In a last pass, each "empty" image received the mask of the closest good artery mask. This procedure was used because images are very close to each other, leading to few structural changes between 2 masks distant from less than 25 images (about 20 μm).

Another analysis was performed to detect branching of secondary arteries. Briefly, we compared a smooth lumen mask with a high precision one to detect protrusion-like branching. By this way, we kept the image number in a file if there was a connected artery in order to skip it during measurements. The lumen mask was then dilated by assuming an extremely thick artery wall, in order to get also the adventitia layer and to be sure to keep the external elastic lamina. In a second step, 2D images were filtered using Frangi vessel enhancement filter[12] to detect tubular structures with a noisy background. The Frangi images were then used as a guideline for a 3D hysteresis thresholding. This second step of detection ensured the possibility to detect the boundary between media/adventitia and also the interlamellar regions, with a good accuracy. In a third and last step, the original image of the artery wall was slightly deblurred with a 5 × 5 Wiener filter and segmented using both masks. Measurements were then carried out by first using a smoothed version of the luminal mask. Orthogonal lines to this mask were used for profiling pixel intensities.

Peak intensities and half-height widths were determined using Matlab-dedicated functions.

The estimation of the thickness and the width of the filamentous structures were performed with bespoke Matlab script using the following procedure. First, an image thresholding level was manually chosen on the basis that (1) it allowed the view of the filamentous structure and (2) modifying its value did not change drastically the measurements, indicating that we used a robust thresholding value. Second, the script segmented 3D regions with contiguous voxels and removed the smallest volumes. The resulting 3D regions were very rough forbidding reliable measurements. Therefore, we created a specific α-shape, around each 3D region, with enough surface tension to smooth the surface and with sufficient accuracy to properly fit the shape. The intersection of the image plane with the α-shape was the geometric representation of the cross-section plane that was then fit with an ellipse. The thickness is the minor axis of the ellipse, and the width is the major axis. About 10k to 75k measurements could be achieved for both width and thickness on each tomogram.

3 | RESULTS

Histological techniques which are commonly used to image tissues suffer from several limitations including the uses of thin sections (3-5 μm) of tissue and hence potential structural alteration during the sectioning process. In contrast, X-ray microcomputed tomography allows imaging of large sample volumes with an excellent resolution relative to the imaged sample size. For instance, the global architecture of a rat carotid artery, and notably elastic lamellae, can be assessed with excellent differential contrast with a laboratory microCT system using absorption contrast in conjunction with phase contrast enhancement.[6] Because the mouse is a commonly used model in exploring age-related disorders, we undertook an exploration of mouse aortic features using X-ray micro-computed tomography allowing the observation and analysis of intramural elastic lamellae as observed previously.[6] We opted for a synchrotron source with inline phase contrast in order to reach sufficient resolution and contrast in unstained tissues without contrasting agents.

We imaged vessels of 3-month-old healthy mice from three strains sharing the same genetic background. That way, observations of differences between the three conditions would not originate from possible genetic variations between strains, but from the conditions themselves, say normal, diabetic, or atherogenic-prone.

Strain C57Bl6J can be considered as a normal mouse; *db/db,* and *ApoE*$^{-/-}$ mice are models for diabetes and atherosclerosis, respectively. All animals were apparently healthy; the diseases could not be detected without anatomopathological approaches.

Aorta from C57Bl6J (control mouse), *db/db* (reference model for diabetes), and *ApoE*$^{-/-}$ (atherosclerosis-prone mouse model) were dissected, washed in PBS, fixed in formalin, and embedded in paraffin. Five samples were prepared for each condition and subsequently imaged at beamline I13-2 of the Diamond Light Source, UK. Each aorta was scanned at three different positions: one in the upper portion of the sample (thoracic), one in the middle, and one near the bottom of the sample (abdominal aorta). The arterial structure was typically imaged over its full volume (up to 1.5 × 1.5 × 2 mm) with an effective voxel size of 830 nm, leading to a typical 26 GB image stack. Images were then automatically segmented by our image analysis program, that detects the lumen and segment the surrounding wall, in order to isolate elastic structures and to measure them.

As shown in Figure 1A, good phase contrast allowed for the identification of arterial features. Except for their size and their very high level of details, due to better contrast and higher resolution, these images were comparable to those obtained formerly for unstained rat vessels using a "laboratory" X-ray source (microfocus tube).[6] However, the high resolution, flux, and coherence provided by the synchrotron source permitted to observe fine details within the fixed block with a very good signal-to-noise ratio. The elastic lamellae, mainly composed of elastin, appear as brightly contrasted objects. Our data are consistent with the results described by Lopez-Guimet and colleagues[7] who also used an X-ray synchrotron source to image aorta from aging healthy and Marfan syndrome model mice.

Although the internal *intima* layer, which is constituted of endothelial cells, is poorly contrasted and cannot be observed, the *media* and *adventitia* layers can be readily identified. The *media* comprises the region between the internal elastic lamella (IEL) and the external elastic lamella (EEL). The outer region of the aorta represents the *adventitia*. Despite their small size, the elastic lamellae present in the arterial wall appeared clearly contrasted from the interstitial and surrounding tissues. The images had a good signal/noise ratio in most cases and, consequently, they were compatible for the automated image processing method we developed in Matlab.

Image stacks that passed the quality control (11 in total: 5 control, 2 *db/db,* and 4 *ApoE*$^{-/-}$) were automatically segmented. This automated step was developed so as to avoid human bias during the segmentation process. Despite possible local noise or lack of contrast, our method allowed the segmentation of key arterial structures (elastic lamellae) throughout the vessel wall. Indeed, the tubular shape of the aorta and the continuity of elastic structures

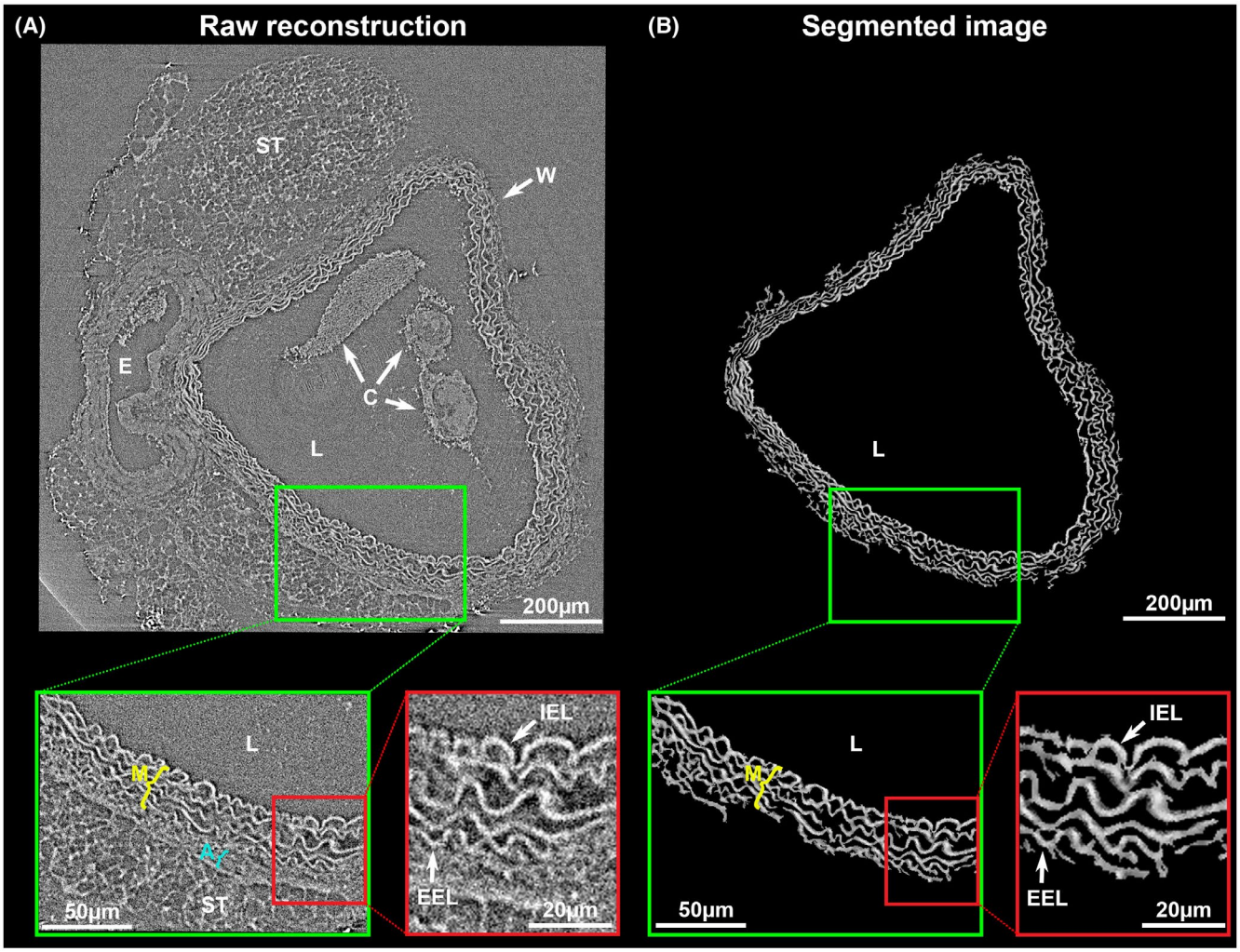


FIGURE 1 Image analysis process. A, Cross-sectional slice from the tomogram of a C57Bl6J sample. Surrounding tissue (ST) and esophagus (E) are visible around the aorta. The aortic wall (W) surrounds the lumen (L) that could contain blood clots (C). Magnifications of the aortic wall show two boundaries: media (M)/adventitia (A) and adventitia/surrounding tissue. Higher magnification of the tomogram reveals the level of noise explaining the difficulty to detect these boundaries. B, Automated segmentation performed by our image analysis program on image A. Elastic structures are isolated from the rest of the image. The boundary between media and adventitia are resolved by analyzing the "local tubular aspect" of the pixels

through each dimension allowed segmentation without any complex assumption.

Figure 1B presents a typical example of the image obtained after this procedure. As can be observed, elastic lamellae are extracted from the image. Magnifications of the segmented image demonstrate that, even in noisy background, the Frangi filter[12] used provides an excellent way to detect the 2D elastic structures and build the corresponding 3D volume (Movie S1). This filter is commonly used to detect vessel-like or tube-like structures and fibers in image data.

In order to have a better understanding of the efficacy of our automated method, we compared the results obtained by our algorithm to those obtained manually. This analysis (Figure S1) demonstrates that the automated and manual methods recognize the same objects (aortic wall). But it also underlines that pixels inside the wall are categorized more efficiently by our automated image processing procedure. In most cases, the differences observed between the two methods concern pixels found at the boundaries of the wall, say in regions where making the decision whether the pixel belongs to the lamella or not is difficult to reach either automatically or manually. Altogether, we estimated that our automated method generates 0.1% "false positive" (kept while it should be deleted) and 1% "false negative" (deleted while it should be kept) pixels (Figure S1). We emphasize here that these pixels are predominantly found at the boundaries of the elastic structures and that they are not very bright. Consequently, they are mostly ignored during the measurement procedures.

Using our algorithm, we were able to extract elastic structures along thousands of images (about 2 mm of

length), which permitted us to detect secondary artery branching along the aorta (Movie S2).

In order to extract relevant information from our segmented images, 2D slices were processed using the same procedure (Figure 2). Our measurements were performed on stacks of 200 consecutive 2D slices belonging to the 11 acceptable mice samples. First, the internal perimeter of the aorta was computed, and orthogonal centripetal segments were drawn along. Depending on the perimeter value, from 200 to 300 segments were drawn (Figure 2A). Along each of those, a pixel intensity profile was computed allowing the identification and measurements of local arterial features (Figure 2B).

For each group of slices, about 50,000 lines were drawn yielding an equivalent number of individual measurements for every single parameter considered. The computed mean values for the 11 mice we considered are reported in Table 1. As our segmentation and analysis methods ensure that all slices were treated the same way, C57Bl6J, *ApoE*$^{-/-}$, and *db/db* results could be compared. They were distributed as follows: 5 C57Bl6J, 4 *ApoE*$^{-/-}$, and 2 *db/db* mice. In the following, statistical comparisons will only be performed between C57BL6J and *ApoE*$^{-/-}$ groups.

At the scale of the artery, the internal perimeter we measure is consistent (about 3 mm) and in good agreement with values reported in the literature[13] for each group. Although we observe a trend for media thickening for *db/db* and *ApoE*$^{-/-}$ mice, we must emphasize that it is not statistically significant (*P*-value .11, Mann-Whitney test). The number of observed lamellae is close to 5 in each case. As can be observed, the measures performed for IEL, intermediate lamellae, EEL, and interlamellar distance vary substantially between individuals and between groups. Nevertheless, these apparent differences between the control and atherogenic mice were not significant: IEL thickness (*P-value* .11), intermediate thickness (*P-value* .06), EEL thickness (*P-value* .06), and interlamellar distance (*P-value* .28). In contrast, if we do not consider the strain as a group, but rather look at the individual measurements, we observe that the IEL is always thicker than the corresponding EEL. This difference is equivalent in all strains for mice having the same age (*P-value* .41).

While significant structural differences were not evident in 2D slices through the synchrotron data, the analysis of the corresponding 3D volumes proved to be very informative. For each series of consecutive images, stacking was performed to create a 3D volume corresponding to the arterial elastic structures (Figure 3, Movie S1). The 3D global organization of elastic structures is in good agreement with former data obtained for rat[6] and mice.[7] The intimal surface presents a rippled aspect (Figure 3A), following the artery main axis with a periodicity of about 220 μm for C57Bl6J mice. This aspect is commonly explained by a partial withdrawal mainly due to the contractility of the artery wall in the absence of an internal pressure. This imaging technique coupled with our segmentation program allowed the observation of secondary artery junctions (Figure 3B) and how elastic structures are locally reorganized to allow connection (Figure 3C).

In order to have greater insights into the 3D global organization of elastic structures, we explored its inner constitution by thresholding pixel intensity. In our imaging modality, pixel intensity is a function of X-ray attenuation

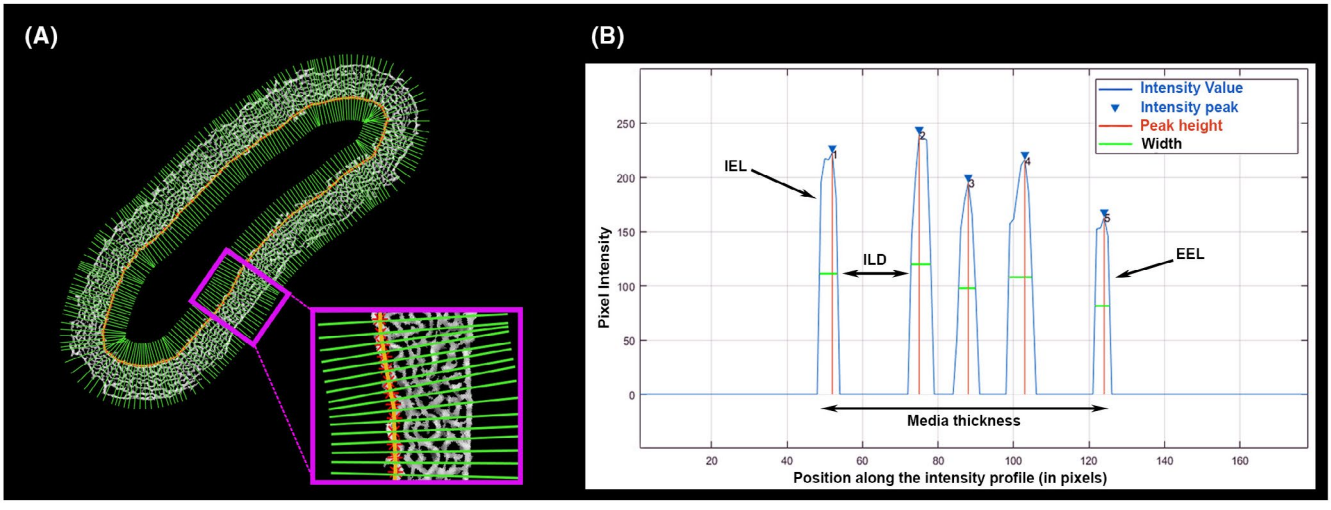


FIGURE 2 Measurements on each 2D section. A, Orthogonal lines (green) based on the luminal mask contour (yellow) are plotted at a distance from each other that abolished the possibility of oversampling. B, Each line is then used to measure pixel intensity and thus find the position of each elastic structure. Their width is measured at half-height of each intensity peak. Interlamellar distance (ILD) is the distance between the end of a lamellae to the start of the next one. So, media thickness is deduced from the start of the IEL to the end of EEL

TABLE 1 Measurements of mice aortic elastic structures

				Lamellae measurements				
					Mean lamella thickness (μm)			
Strain	Location	Mean internal perimeter (μm)	Mean media thickness (μm)	Mean number of lamellae	IEL	Intermediate	EEL	Inter-lamellar distance (μm)
C57Bl6J	T	3113	52.09	4.48	5.20	4.69	4.96	12.49
	T	3258	59.27	4.62	6.34	5.27	4.74	13.77
	A	2629	68.28	5.74	6.08	5.95	5.57	11.50
	A	3208	59.64	5.10	4.74	4.70	4.60	12.19
	A	3103	50.31	4.60	5.00	4.60	4.62	11.95
ApoE$^{-/-}$	T	2694	63.45	5.29	5.80	5.74	5.54	12.55
	T	3700	64.19	5.09	6.70	6.03	5.88	13.11
	T	2876	75.44	5.68	8.86	7.98	7.66	13.96
	A	2595	62.18	4.89	6.31	5.42	5.19	12.02
db/db	T	3072	72.23	5.73	7.35	7.45	7.24	12.17
	A	3020	62.95	4.72	6.52	5.51	5.56	13.76

Note: For each individual mouse (line), the reported numbers correspond to the average of measurements performed on 200 consecutive slices for the considered parameter (about 50'000 measurements). These slices could be located in the upper or lower part of the aorta. Location refers to the scan position along the aorta: T (thoracic segment) and A (abdominal segment).

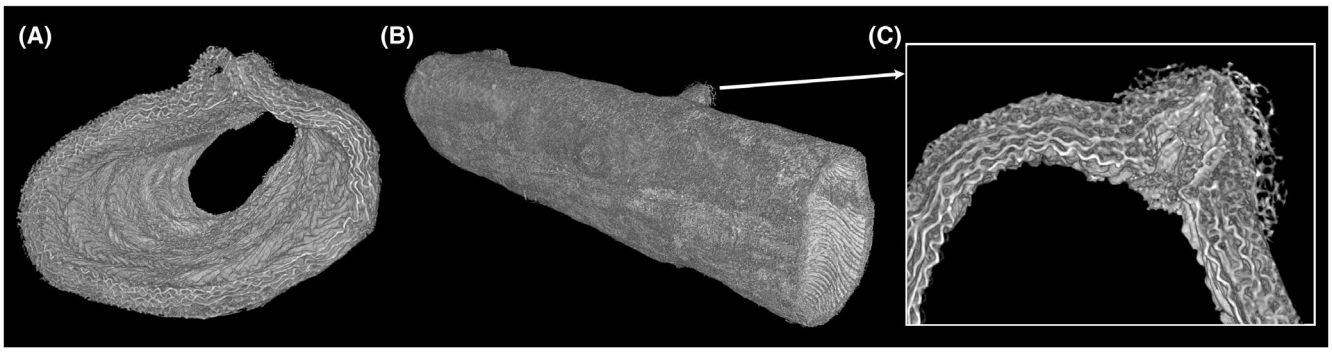


FIGURE 3 3D reconstruction of C57Bl6J aorta elastic structures. A, Surface render of X-ray tomogram (total length 1.78 mm). The internal surface is rippled, with a periodicity of 220 μm, due to the lack of internal pressure. B, Global view of the 1.78 mm aortic segment. A secondary artery junction is zoomed on figure (C) where a cross-sectional view shows the elastic tissue local reorganization

and phase-shift. With our samples, we could visualize the internal features of elastic lamellae.

Upon increasing the threshold level (Movie S3), a network of "filamentous" structures was revealed in volumetric views (Figure 4A). At 90%, only the 10% brightest pixels are kept. The unraveled network is therefore a highly phase-contrasted material. A closer look at its organization (Figure 4B) shows that this network has a braided aspect with possibly several layers (Movie S4). Given its overall organization, this lattice-like filamentous network seems to constitute a "scaffold" built inside the arterial elastic structures (Figure 4C). The filamentous structures (several pixels across) are apparently distributed evenly along the circumference of the lamellae and follow the major axis of the aorta (Figure 4B,C, Movie S4). Importantly, we observed these features for all three strains (Movie S5) at three months old.

In order to obtain more information about these structures, we developed an image analysis tool to isolate segments of these filaments, colorize them (Figure 5, left), and estimate their local thickness (Figure 5, middle) and width (Figure 5, right), in each image plane. Results exhibit a Gaussian aspect for both measurements allowing comparison. Average thickness measurements corresponded to the values obtained for mean lamellar thickness (Table 1), confirming the increase we observed for *db/db* samples. This point suggests that these ribbon-like structures occupy the whole thickness of the elastic lamella. The measurement of their widths also demonstrates higher values for *db/db* samples (about 32 μm) as

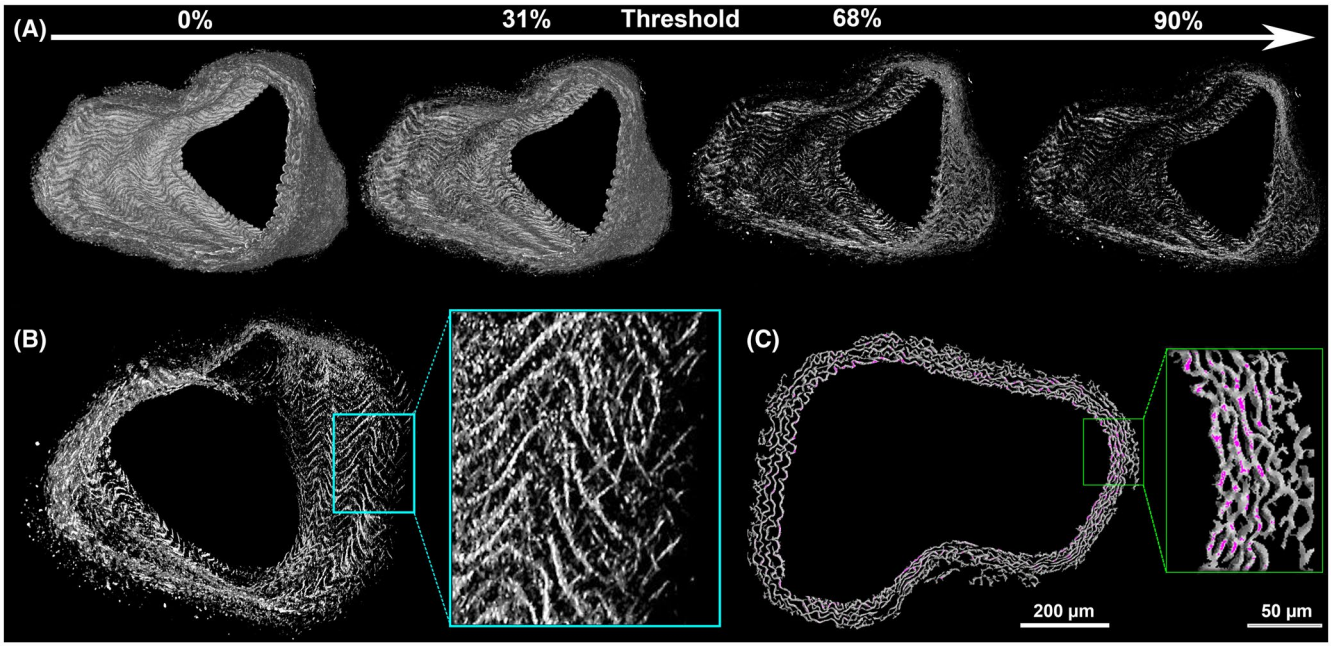


FIGURE 4 Exploring the elastic structure of mouse aorta wall reveals a braided network inside the elastic lamellae. A, Increasing the lower voxel intensity threshold reveals a network formed of higher phase-contrasted elastin. B, 90% thresholding value shows details of the network and its alternate braiding as visible on magnifications where filaments appear to be differentially oriented regarding to their depth inside the artery wall. C, Filaments (pink) are not localized in any particular areas of the lamellae as visible in magnification

compared with C57Bl6J and $ApoE^{-/-}$ (about 25 µm) mice. More than the absolute values, the ratio between the width and the thickness seems to be conserved in each strain at a value of approximatively 3.75 ± 0.25 µm. Collectively, our results suggest that these filamentous structures are better described as ribbons. This point is illustrated in movies S6, S7, and S8.

4 | DISCUSSION

Applying synchrotron X-ray microcomputed tomography with unstained soft tissues combined with a suitable image analysis workflow granted access to information unreachable using other imaging methods (Figures 1 and 3). Indeed, having a large image field, a good resolution, and an excellent signal to noise ratio required for such tissues permitted to obtain informative image stacks. Nevertheless, powerful computational equipment was required to process, measure, and visualize them. The strength of our method lies in the fact that it is able to measure intramural features, notably the thickness of lamellae and the interlamellar distance and we point out that these reported values (Table 1) are average values from thousands of measurements on each sample.

Because it presents an amorphous appearance when observed by transmission electron microscopy, elastin has long been thought to be unstructured.[14] But, quick freeze deep etch images of growing elastic fibers show that rather than being an amorphous material, elastin is made of a densely packed but relatively disordered arrangement of filamentous substructures.[14] The high phase-shifting filamentous substructures we observe within elastic lamellae (Figure 4) could be relevant of this organization. Kozel and Mecham[14] have stressed that elastin internal features are preserved when the samples are prepared using soft methods. We therefore avoided sample labeling/staining for our experiments.

To our knowledge, the lattice-like network we observe has never been reported despite numerous attempts to provide 3D micro and nanostructure images that directly address elastic fiber/elastic lamellae ultrastructure.[15] The filamentous structures we observe are gradients of matter that spread over hundreds of microns along the axis of the artery. Their observation is made possible by the conjunction of the following four requirements: 3D imaging over relatively large volumes (a key strength of microCT), a large field size associated to a good resolution and phase-contrast. This explains why these features were not observed by 2D imaging approaches.

The wavy aspect of this network could suggest that it may be caused by internal pressure loss and/or 3D reconstruction artifacts. The loss of arterial pressurization is commonly known to be the cause of the wavy appearance of ex-vivo arterial sections. Nevertheless, the waves

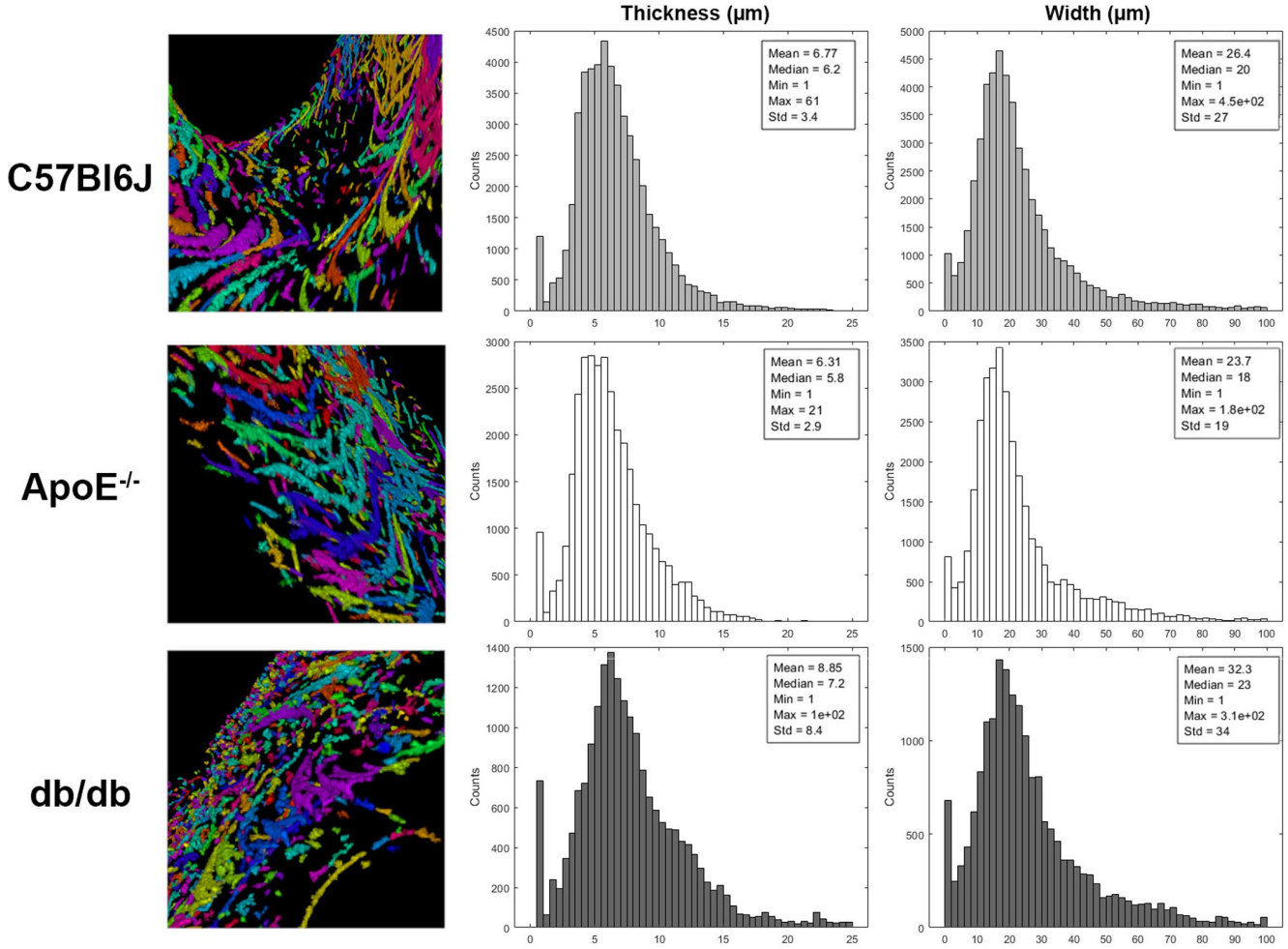


FIGURE 5 Measurements of filamentous structures inside the arterial walls. Colored images correspond (left column) to a detailed view of the individualized filamentous structures, one color per 3D continuous element of structure of the corresponding mouse strain. The filamentous structures appear like "ribbons" rather than strings (see movie S6, S7, and S8). The histograms correspond to the thickness (middle column) and the width (right column) of ribbons. They were drawn from 20k to 50k measurements obtained for each single sample of the corresponding mouse strain

observed on the intimal elastic lamella also exist at physiological pressure.[16] Hence, pressure is not the sole origin of the waviness, and wavy aspect appears as an intrinsic property of the aortic elastic material. The "waves" of the filamentous network are parallel to those on the intimal surface (Figure 3) but they are not strictly linked to a specific position in the circumvolution observed in cross section in elastic lamellae (Figure 4C). As an example, filaments are not always located on the ripples.

With regards to 3D reconstruction and visualization, it is important to note that our imaging program segments images and does not modify the pixel intensity of the original tomogram. However, as 3D visualization is a critical step in detecting these filamentous structures, we have also demonstrated that three alternative programs (Matlab, ImageJ, and Amira) also visualize these structures. And as ripples and filamentous structures do not fully colocalize, we conclude that they do not originate from a 3D visualization artifact. Collectively our observations provide evidence for the existence of a previously unreported internal structure in arterial elastic lamellae, however future studies will be required to confirm these observations using alternative experimental approaches.

The bright filaments of the lattice-like network indicate high local phase-contrast in the absence of labeling. This intense signal modulation may be due to localized differences in X-ray attenuation (absorption and/or scattering) and/or phase-shift. However, it is not possible to determine from our data which mechanism is the key mediator of these modulations. Within elastic lamellae, material heterogeneity (and hence heterogeneity in X-ray/tissue interactions) could be due to differences in density and/or composition (ie., differentially cross-linked "amorphous"

elastin or regions enriched in microfibrillar components). Alternatively, as the punctual presence of collagen fibers has been reported inside elastic structures in AFM explorations,[17] this high contrast could also originate from collagen fibers. Future work should use alternative (and potentially higher resolution) approaches such as serial block-face SEM to probe the internal structures of elastic.

Although the high resolution of our images permitted the automatic measurements of arterial structural parameters for all three murine strains, we did not detect any significant morphological differences. Two interpretations are possible. First, due to low sample number and intrinsic variability, structural differences are present but not detected statistically. Second, mice examined in this study may be too young to have developed significant age-related modifications. Nevertheless, there is a trend for differential organization between the normal and pathological models which may be more clearly detected by working on a larger panel and considering identical arterial regions. It is clear however, that the complex and interwoven network which our work reveals is a consistent feature throughout the whole aorta; its geometry and organization within the wall are comparable to the "copper braid" that reinforces, softens, and confers resilience to a cable. Thus, we hypothesize that this network could contribute to the mechanical properties of the artery.

Our work demonstrates that synchrotron X-ray microcomputed tomography with inline phase contrast can reveal mouse aortic elastic structures images at millimeter scale with an effective pixel size lower than a micron, without using labeling agents. This imaging method coupled to automated image analysis software allowed us to reveal a hidden 3D braided network that may reinforce the arterial wall. We were also able to measure fine details within the arterial wall. Our feeling is that these measurements could be used to detect subtle and discrete changes occurring in pathological states during the asymptomatic phases of the diseases (atherosclerosis or diabetes). Further experiments in this direction are underway.

The resolution power of the X-ray synchrotron source coupled to automated analysis algorithm opens new perspectives in the exploration of complex biological assembly and structures such as those constituting the extracellular matrix. For instance, this imaging method could be used to explore the influence of aging on arterial structure and/or vascular disease onset and progression in various models. Indeed, our work demonstrates that visualization of submicrometric details in unstained and fixed soft tissues is possible and that our approach could be adapted and applied to tissues where elastic fibers integrity is a major concern (skin, ligaments and lung).

ACKNOWLEDGMENT

The authors gratefully acknowledge the assistance provided by Dr CM Disney, Dr R Bradley, Dr K Madi, and Dr M Yusuf during data collection. The chair MAgICS is acknowledged for financial and technical support. This work was funded by DLS under MT12776 proposal. ABZ and AG were funded by the University of Reims Champagne-Ardenne. DRRT of Champagne-Ardenne funded this work *via* the "Projet Incitatif Amont" program. The financial support of Centre National de la Recherche Scientifique (CNRS) is also acknowledged.

CONFLICT OF INTEREST

The authors declare no competing financial interests.

AUTHOR CONTRIBUTIONS

ABZ and AG contributed equally to this work by programming, performing computational experiments, and contributing to article redaction. AW, SB, and BRC prepared samples. AW, LD, AB and MJS imaged samples at Diamond Light Source (proposal MT12776), with assistance from Dr K Wanelik. JJ, RC, and PB provided analytical tools. MD supervised work and arranged funding for the project. LD and MJS conceived the imaging procedure and assisted with article planning. SA conceived the image analysis program, supervised the work, and wrote the article with LD.

REFERENCES

1. Fhayli W, Boëté Q, Harki O, Briançon-Marjollet A, Jacob M-P, Faury G. Rise and fall of elastic fibers from development to aging. Consequences on arterial structure-function and therapeutical perspectives. *Matrix Biol*. 2019;84:41-56. https://doi.org/10.1016/j.matbio.2019.08.005
2. Mithieux SM, Weiss AS. Elastin. *Adv Protein Chem*. 2005;70:437-461.
3. Shapiro SD, Endicott SK, Province MA, Pierce JA, Campbell EJ. Marked longevity of human lung parenchymal elastic fibers deduced from prevalence of D-aspartate and nuclear weapons-related radiocarbon. *J Clin Invest*. 1991;87(5):1828-1834.
4. O'Rourke MF, Safar ME, Dzau V. The cardiovascular continuum extended: aging effects on the aorta and microvasculature. *Vasc Med*. 2010;15(6):461-468. https://doi.org/10.1177/1358863X10382946
5. Shearer T, Bradley RS, Hidalgo-Bastida LA, Sherratt MJ, Cartmell SH. Three-dimensional visualisation of soft biological structures by X-ray computed micro-tomography. *J Cell Sci*. 2016;129(13):2483-2492. https://doi.org/10.1242/jcs.179077
6. Walton LA, Bradley RS, Withers PJ, et al. Morphological characterisation of unstained and intact tissue micro-architecture by X-ray computed micro- and nano-tomography. *Sci Rep*. 2015;5(1). https://doi.org/10.1038/srep10074
7. López-Guimet J, Peña-Pérez L, Bradley RS, et al. MicroCT imaging reveals differential 3D micro-scale remodelling of the murine aorta in ageing and Marfan syndrome. *Theranostics*. 2018;8(21):6038-6052. https://doi.org/10.7150/thno.26598

8. Rau C, Wagner U, Pešić Z, De Fanis A. Coherent imaging at the diamond beamline I13. *Phys Status Solidi A*. 2011;208(11):2522-2525. https://doi.org/10.1002/pssa.201184272
9. Pešić ZD, Fanis AD, Wagner U, Rau C. Experimental stations at I13 beamline at diamond light source. *J Phys Conf Ser*. 2013;425(18):182003. https://doi.org/10.1088/1742-6596/425/18/182003
10. Titarenko V. Analytical formula for two-dimensional ring artefact suppression. *J Synchrotron Radiat*. 2016;23(6):1447-1461. https://doi.org/10.1107/S160057751601479X
11. Schneider CA, Rasband WS, Eliceiri KW. NIH Image to ImageJ: 25 years of image analysis. *Nat Methods*. 2012;9(7):671-675. https://doi.org/10.1038/nmeth.2089
12. Frangi AF, Niessen WJ, Vincken KL, Viergever MA. Multiscale vessel enhancement filtering. In Wells WM, Colchester A, Delp S (Eds.), *Medical image computing and computer-assisted intervention — MICCAI'98* (pp. 130–137); Springer; 1998.
13. Wheeler JB, Mukherjee R, Stroud RE, Jones JA, Ikonomidis JS. Relation of murine thoracic aortic structural and cellular changes with aging to passive and active mechanical properties. *J Am Heart Assoc*. 2015;4(3). https://doi.org/10.1161/JAHA.114.001744
14. Kozel BA, Mecham RP. Elastic fiber ultrastructure and assembly. *Matrix Biol*. 2019;84:31-40. https://doi.org/10.1016/j.matbio.2019.10.002
15. Oconnell M, Murthy S, Phan S, et al. The three-dimensional micro- and nanostructure of the aortic medial lamellar unit measured using 3D confocal and electron microscopy imaging. *Matrix Biol*. 2008;27(3):171-181. https://doi.org/10.1016/j.matbio.2007.10.008
16. Walton LA. *From molecules to tissues: Characterising the relationship between structure and function in ageing arteries*. University of Manchester; 2014.
17. Graham HK, Hodson NW, Hoyland JA, et al. Tissue section AFM: in situ ultrastructural imaging of native biomolecules. *Matrix Biol*. 2010;29(4):254-260. https://doi.org/10.1016/j.matbio.2010.01.008

SUPPORTING INFORMATION

Additional Supporting Information may be found online in the Supporting Information section.

How to cite this article: Ben Zemzem A, Genevaux A, Wahart A, et al. X-ray microtomography reveals a lattice-like network within aortic elastic lamellae. *FASEB J*. 2021;35:e21844. https://doi.org/10.1096/fj.202100323RR